Predicted Intent Inferred from Real-time Rendezvous and Proximity Behavior

Thomas Kelecy

The Stratagem Group, Aurora, CO USA

Shawn Abernethy, Frank Jones, Emily Gerber and Hannah Wurzel

The Stratagem Group, Aurora, CO USA

ABSTRACT

Closely Spaced Object (CSO) relative motion behavior can be categorized into the following classes: (a) normal close proximity operational behavior between CSOs, (b) cooperative Rendezvous and Proximity Operations (RPO) behavior, (c) inadvertent RPO behavior due to a satellite anomaly, or (d) provocative RPO behavior (a threat). In addition to the CSO classes, a 5th class is included in the analysis: (e) relative motion between adjacent GEO satellites during normal operations. The goal of this work is to derive and demonstrate the application of a set of observable Indications and Warnings (I&W) metrics using classification techniques that infer the intent of RPO behavior from observed relative motion. This behavior driven intent is intended to be applied in near real-time from ground and/or space-based Electro-Optical (EO) imagery sources. Relative observations extracted from the imagery are simulated to develop Artificial Intelligence (AI) spatiotemporal models that classify the behavior with the primary goal being to demonstrate the ability to quickly discriminate between natural, cooperative and threatening RPO activities. The innovation of this work is the application of AI to "spot" the relative behavior that might indicate a threatening RPO activity using real-time image data without the need for detailed tracking analytics used in traditional orbit estimation and data association processes. The AI spatiotemporal model delivers 86% accuracy when classifying RPO activity behavior for either ground or space-based observations. The best results are obtained when a combined set of ground and space-based observations are used. The data partitioning strategy for training and testing is also of crucial importance. The primary benefit to space safety is near real-time detection and prediction of threats based on observed relative behavior of Resident Space Objects (RSOs) to support rapid execution of Courses of Action (CoA).

Keywords: Rendezvous & Proximity Operations (RPO); Closely Spaced Objects (CSO); machine Learning (ML).

1. INTRODUCTION

RPO activities in space are becoming more common. Multiple organizations are increasing the number of demonstrations and deployments of space-based servicing missions and scientific activities which apply proximity maneuvers [1] [2]. Missions are under development to demonstrate retrieval and removal of large defunct satellites and other orbital debris [3]. At the same time, some nations have also demonstrated RPO capabilities that might warrant safety and security concerns [4]. The work presented in this paper intends to demonstrate the ability to discriminate between "expected" vs. "unexpected" RPO behavior from observing the relative motion between satellite detections derived from Electro-Optical (EO) imagery.

The mathematics for modeling and predicting relative motion are well known [5] [6], and the technologies that support such missions involving docking are becoming more mature [1] [2]. However, recent non-cooperative RPO events illustrate examples of activities where unknown satellites operating in close proximity to key assets could result in disruptive, if not catastrophic, consequences for space operators [4] [7]. The goal is to use ground and space-based tracking and processing resources to provide advanced warning for hazards that might result from proximity operations. However, there are known challenges with tracking and data association of CSOs when tracking uncertainties do not permit unambiguous discrimination between objects of interest, hence the motivation to derive intent from relative motion derived from unassociated detections. Also, when an RSO has little or no tracking information, reliable trajectory prediction becomes limited or not feasible.

The primary objective of this work is to demonstrate the use of Machine Learning (ML) to characterize RPO behavior as observed from fundamental tracking data into one of the following categories: (a) normal operations: relative

motion as dictated by the natural environmental factors (Earth gravity, drag, solar radiation, third-body), (b) cooperative RPO behavior: RPO activity such as servicing missions or scientific demonstrations, (c) satellite anomaly: anomalies where loss of control of one satellite results in close conjunctions with another, and (d) provocative behavior (threat): intentional maneuvering of a satellite with the intent of performing surveillance and/or causing intentional interference (or worse) to another satellite. The military benefit is the ability for rapid determination of threats based on observed relative behavior that can support I&W responses, even in the absence of accurate tracking and association.

2. PROBLEM STATEMENT AND ASSUMPTIONS

The primary observations to be examined are EO imagery. Exploitation of additional measurements such as range and RF signals can be examined in future work. Other metadata, such as, knowledge of the country of origin for satellites and whether they are active/operational, or debris is also to be considered. Different classes of RSOs will exhibit different dynamic attributes that will affect the observed relative motion. A range of observing geometries for the image generation are to be simulated to verify results are not biased by limited observing geometry. As previously stated, no assumptions are made regarding the association of the data to an individual satellite in the RPO formation, except when each set of measurements on the two objects can be distinguished so that intent can be inferred from the relative motion behavior. ML, information metrics, Bhattacharya distance, and other techniques are examples of approaches that could be used to determine the effectiveness in the intent inference. A successful technique would provide timely I&W of nefarious RPO activities without a priori tracking information. The capability would provide timely I&W if nefarious RPO activities were taking place without the need for immediate detailed tracking and association results.

A key technical step in this work is defining scenarios representative of the following four categories which are also illustrated in Figure 1:

(a) Normal CSO Operations: This category of behavior contains the "Normal" operational RPO activities. Normal operations occurs when two or more RSOs get close to each other as a matter of course, e.g., their operational orbits result in "apparent" close proximity to each other. For example, within the ANIK cluster there are several RPO activities that occur over a 24-hour orbital cycle. A time history of this relative motion would include station-keeping maneuvers and be indicative of "expected" operational behavior.

(b) Cooperative RPO Behavior: This category of behavior contains the "Cooperative" operational RPO activities such as Mission Extension Vehicle (MEV) servicing or International Space Station (ISS) resupply docking. These cooperative RPO behaviors follow prescribed maneuver sequences and proximity docking protocols. RPO activities can be defined in terms of drift, proximity, and docking phases. Each of these phases are accompanied by specified maneuvers and relative orbit characteristics.

(c) Satellite Anomaly: This category of behavior contains the RPO activities that result from a satellite which is no longer responding to operator input as expected. Such a satellite anomaly occurred with GALAXY-15 when a solar weather event caused an on-board anomaly resulting in loss of control [8]. In this case the uncontrolled satellite moves into the proximity of neighbor satellites as the result of natural perturbation forces. Two known "gravitational wells" exist around the Geosynchronous Earth Orbit (GEO) belt which cause uncontrolled satellites in this regime to drift, or more appropriately, oscillate about these wells with a period of days to weeks. A system failure caused GALAXY-15 to lose station-keeping capability and drift out of its allocated slot while continuing to broadcast signals during the uncontrolled drift which resulted in RF interference with other GEO communications systems. This example underscores the importance for early and accurate RPO behavior I&W for maintaining space operations.

(d) Provocative Behavior (Threat): This category of behavior is characterized by any RPO that is purposely performing in an adversarial manner: either physically threatening to a space asset or threatening due to the collection of intel. The Russian LUCH (OLYMP) satellite recently had an interaction with the operational Intelsat satellites [4]. This is one of several instances where the LUCH satellite maneuvered around the GEO belt and stationed itself near other operational assets. Without clear coordination between operators, this type of activity poses a hazard, not only to the targeted satellite, but also to other nearby satellites which would be at risk if a collision were to occur.

(e) Normal Operations Between Adjacent GEOs: This behavior is included as a baseline "normal non-CSO/RPO" case where the relative motion may look similar to CSO and RPO behavior, but the separation distances remain consistent with the operational standards established for maintaining a safe operational separation distance in the GEO orbit regime,

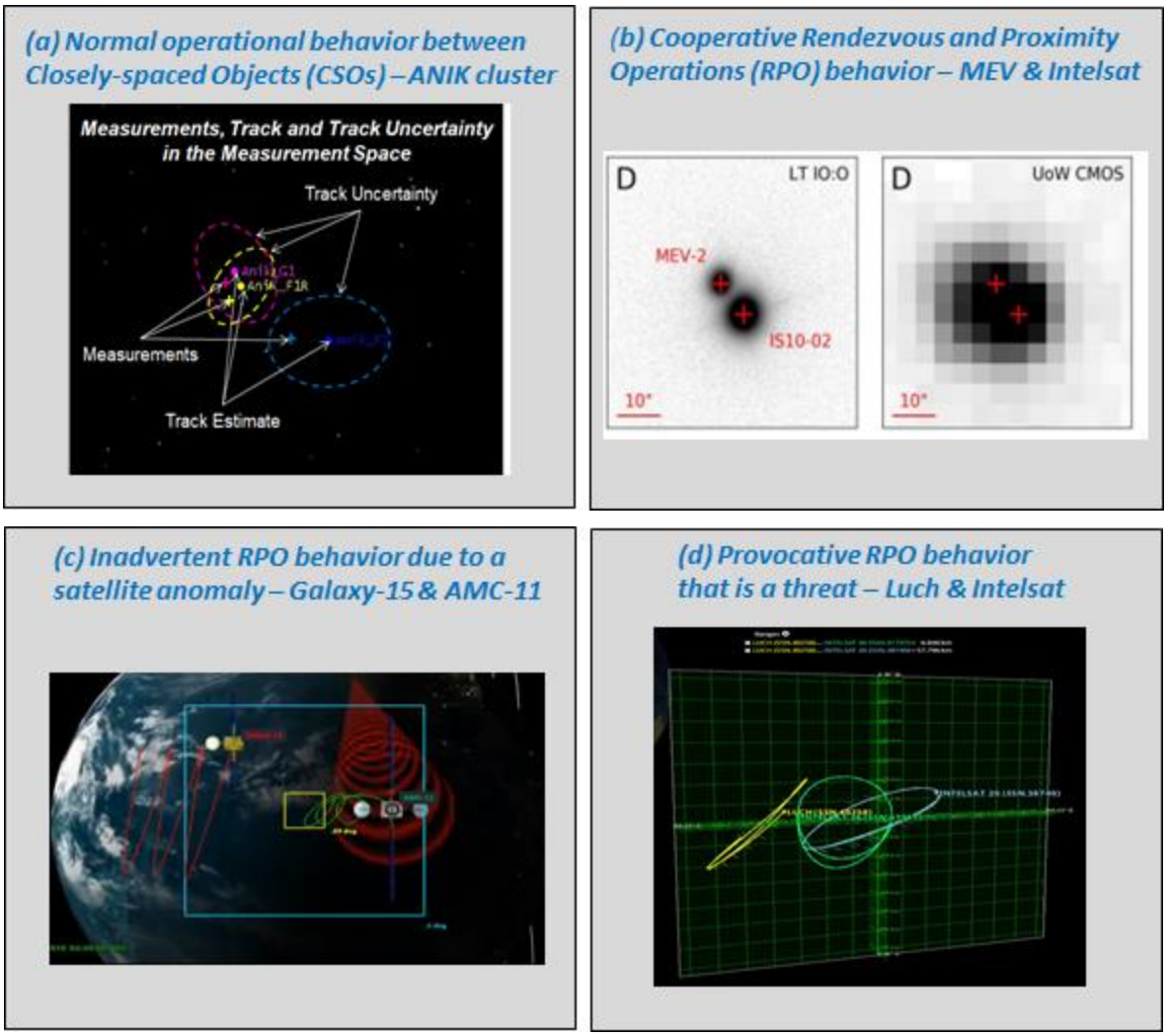

Figure 1. Four CSO use-cases for behavior classification [1] [4] [9] [8]

This work establishes metrics to support quantification of the importance, urgency, and uncertainty (confidence and likelihood) of RPO behavior characterization to support I&W processes for discriminating threats vs. normal behavior posed by observed RPO activities [10]. The goal of this study is to classify simulated RPO behavior detection performance built around an encoder from a Transformer. Transformers are a top-performing multivariate time series regression and classification technique [11].

3. SIMULATED OBSERVATIONS AND TEST CASES

The sensor and image processing are going to be represented by simulated images that are derived from the use cases. Locations of the ground/space-based sensor and target RSO are going to be varied in the orbital modeling to verify diversity of geometry and adherence to the various physics-based orbital and lighting constraints that would be required for actual image measurements. The approach used for simulation of the relative motion metrics derived from EO images is illustrated in Figure 2. The Two-line Element (TLE) histories for the specific use cases that define the classes of relative motion behavior were identified and downloaded from Space Track [12]. These are used to generate J2000 Cartesian position and velocity states that served as the basis for the relative motion dynamics. These are combined with randomly selected ground or space sensor locations and epochs to generate randomized data sets having diverse observing geometries and observing constraints derived from the lighting conditions that are present around the selected epoch.

Examples for the ANIK-F1 vs. ANIK-F1R motion, INTELSAT-901 vs. MEV-1, AMC-11 vs. GALAXY-15 and INTELSAT-36 vs. LUCH (OLYMP) are shown in Figures 3, 4, 5, and 6, respectively. The Radial, In-track and Cross-

track relative position and velocities are plotted on the left whereas range range-rate between each pair of RSOs is shown on the right. At a glance, these plots indicate the unique relative motion attributes associated with each use case. The ANIK case shows periodic relative motion in close proximity, the MEV case shows the approach maneuvers and docking, the GALAXY-15 case shows the drift towards and then away from AMC-11, and finally the LUCH case shows the maneuver up to, loitering around, then maneuvering away from INTELSAT-36. Note, the relative motion contains attributes that the cases have in common, e.g., variations having periodicities on the order of the 24-hour orbit periods, and elements that are quite distinct such as docking, drift, and proximity maneuvers. These are discussed more in the subsequent section. The processes encompassed by the blue box are used to generate the random trial samples for the observation dataset.

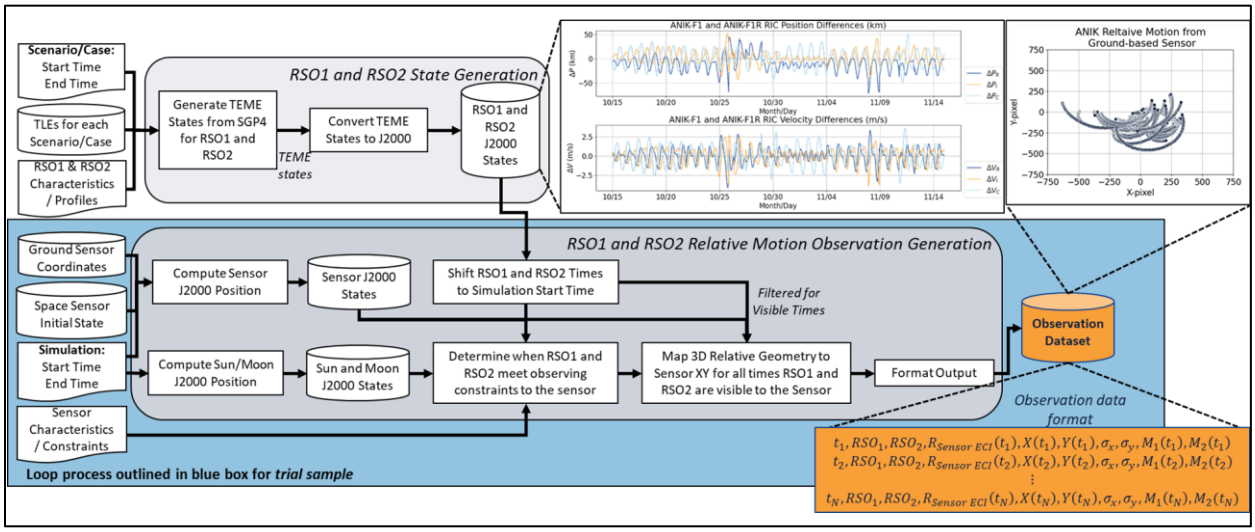

Figure 2. Simulated observation processing

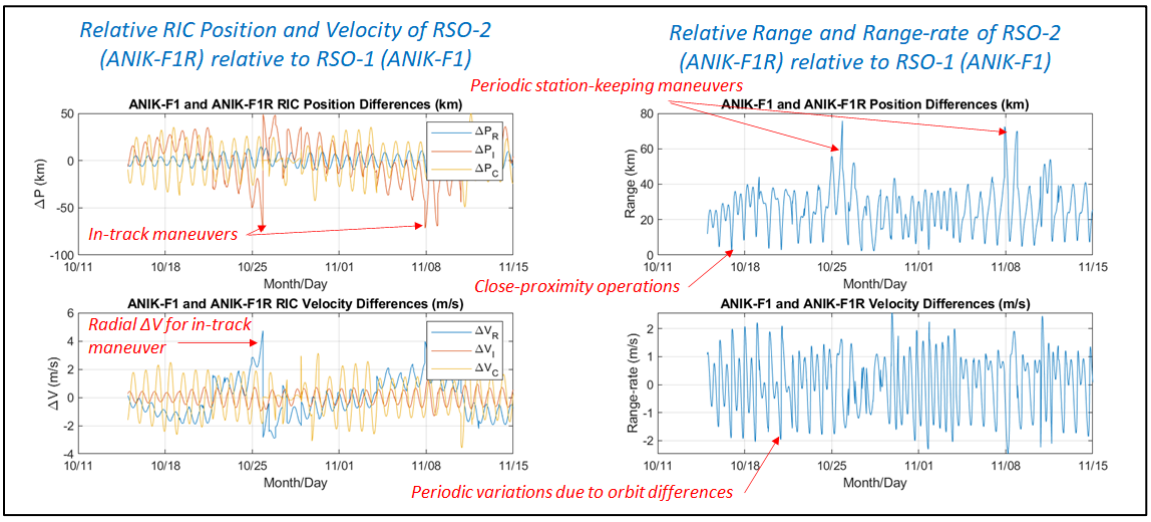

Figure 3. ANIK-F1 and ANIK-F1R RIC Position/Velocity (left) and Range/Range-rate (right)

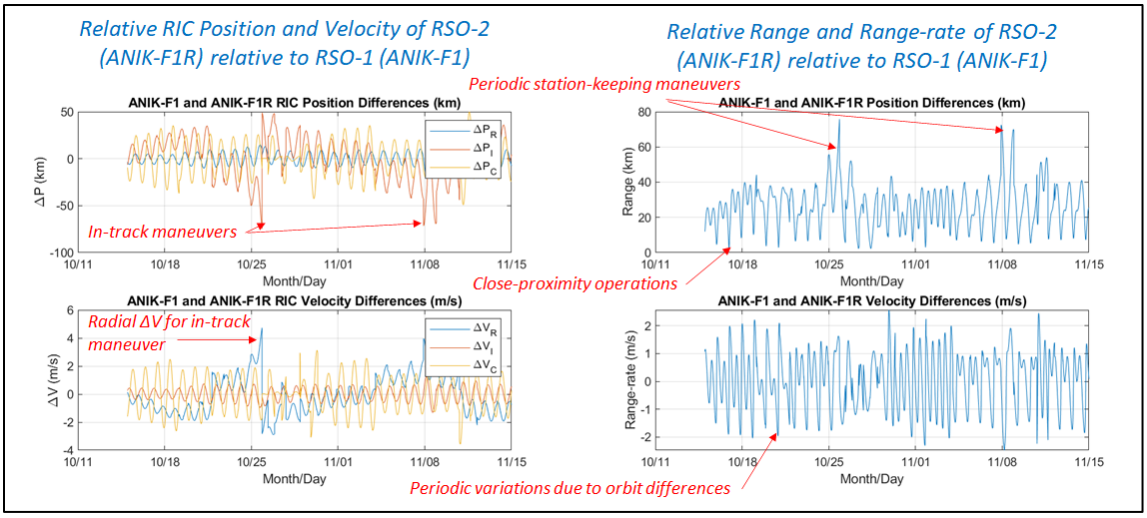

Figure 4. INTELSAT-901 and MEV-1 RIC Position/Velocity (left) and Range/Range-rate (right)

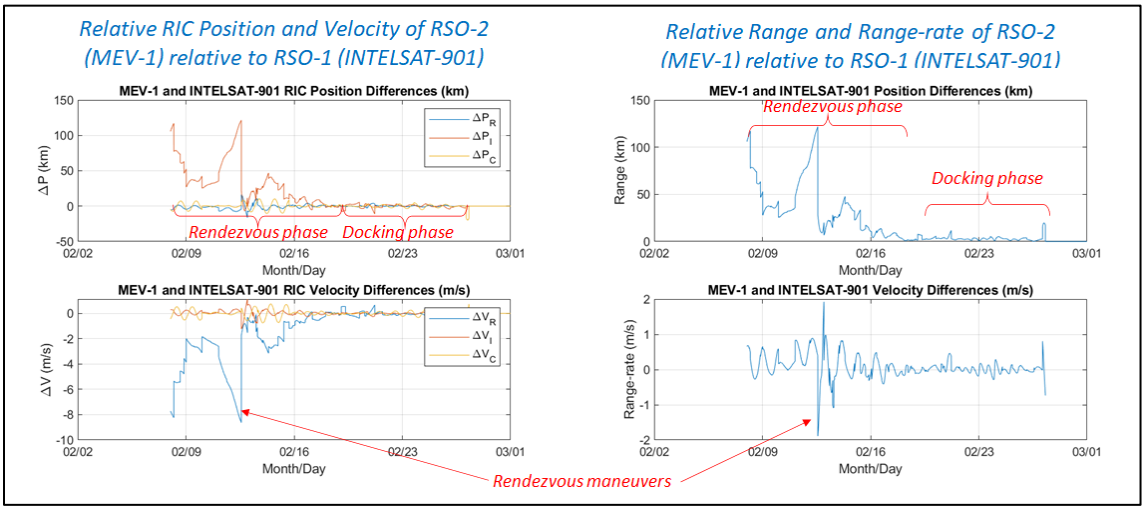

Figure 5. AMC-11 and GALAXY-15 RIC Position/Velocity (left) and Range/Range-rate (right)

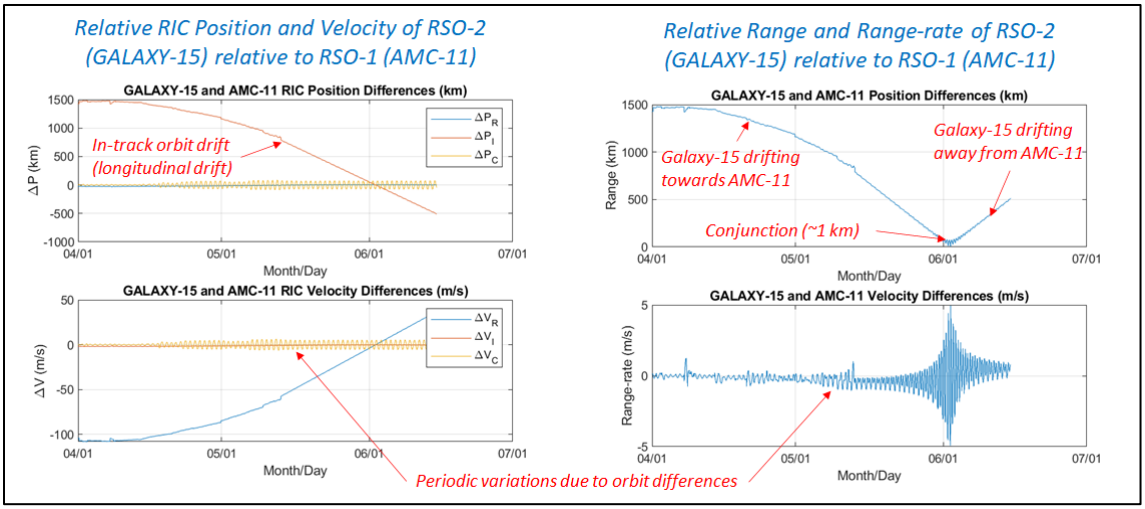

Figure 6. INTELSAT-36 and LUCH (OLYMP) RIC Position/Velocity (left) and Range/Range-rate (right)

Each of the state histories from which the observations are derived has a specified duration and given a 5-minute sampling, determines the number of state data points. These are summarized in Table 1 below where the 4 primary RPO scenarios, plus the "normal" (NORM) behavior for adjacent operational GEOs, are identified with the specific cases identifying the two RSOs for which data were generated.

Table 1. Summary of data and samples by scenario and use case

Scenario		Duration (days)	# State Points	# Trial Samples	# Of Observations
ANIK	**Normal close proximity operations**				
	Case 1: ANIK-F1 and ANIK-F1R	31	8929	100	3100
	Case 2: ANIK-F1 and ANIK-G1	31	8929	100	3100
	Case 3: ANIK-F1R and ANIK-G1	31	8929	100	3100
MEVS	**Cooperative docking**				
	Case 1: MEV-1 and INTELSAT-901	22	6337	100	2200
	Case 2: MEV-2 and INTELSAT-1002	30	8641	100	3000
GALAXY15	**RSO anomaly**				
	Case 1: GALAXY-15 vs. AMC-11	75	21601	500	37500
LUCH	**Provocative behavior**				
	Case 1: LUCH and INTELSAT-36	60	17281	100	6000
	Case 2: LUCH and INTELSAT-905	91	26209	100	9100
NORM	**Normal (non-RPO) GEO operations**				
	Case 1: INTELSAT-901 and SKYNET-5C	30	8641	100	3000
	Case 2: ANIK-F1R and ECHOSTAR-17	31	8929	100	3100

These Cartesian states serve as inputs into the process used for generating the simulated EO detections used for training, validation and testing the classification techniques. The observations are derived from the RSO state vectors,

and the sensor state as illustrated in Figure 7 where the relative motion is mapped to the sensor frame through the appropriate coordinate transformations. The image plane is centered on the "primary" RSO (RSO-1), and the relative coordinates the secondary RSO (RSO-2) is computed based on the sensor viewing geometry, field-of-view and lighting conditions.

The following observation constraints are applied to each trial set of EO observations:

- **Line-of-site**: Each RSO must be in the unobstructed line-of-site from the sensor.
- **Sun exclusion**: The sun must be outside of the designated exclusion angle relative to the sensor line-of-site to the primary RSO being tracked (30°).
- **Moon exclusion**: The moon must be outside of the designated exclusion angle relative to the sensor line-of-site to the primary RSO being tracked (15°).
- **Earth limb exclusion**: An RSO line-of-site from the sensor must be greater than a designated limb angle (15°).
- **Sensor field-of-view**: Both primary and secondary RSOs must be within the designated sensor field-of-view (0.35° cone angle).
- **Minimum range**: The primary RSO must be greater than a specified minimum range relative to a space-based sensor (6482 km).
- **Magnitude limit**: Each RSO must be greater than the minimum visual magnitude detection limit (18 Mv) as determined by the range, phase angle and size of RSO (diffuse sphere model: RSO-1 = 0.5 m, RSO-2 = 1 m).
- **RSOs sunlit**: Each of the RSOs must be illuminated by the sun.
- **Sensor lighting**: The ground-based sensor must be in dark (no lighting constraint for space-based).
- **Weather and sampling**: There are assumed to be no weather outages and sampling is at 300 seconds (5 minutes) when RSO is visible to sensor and meets all other observation constraints.

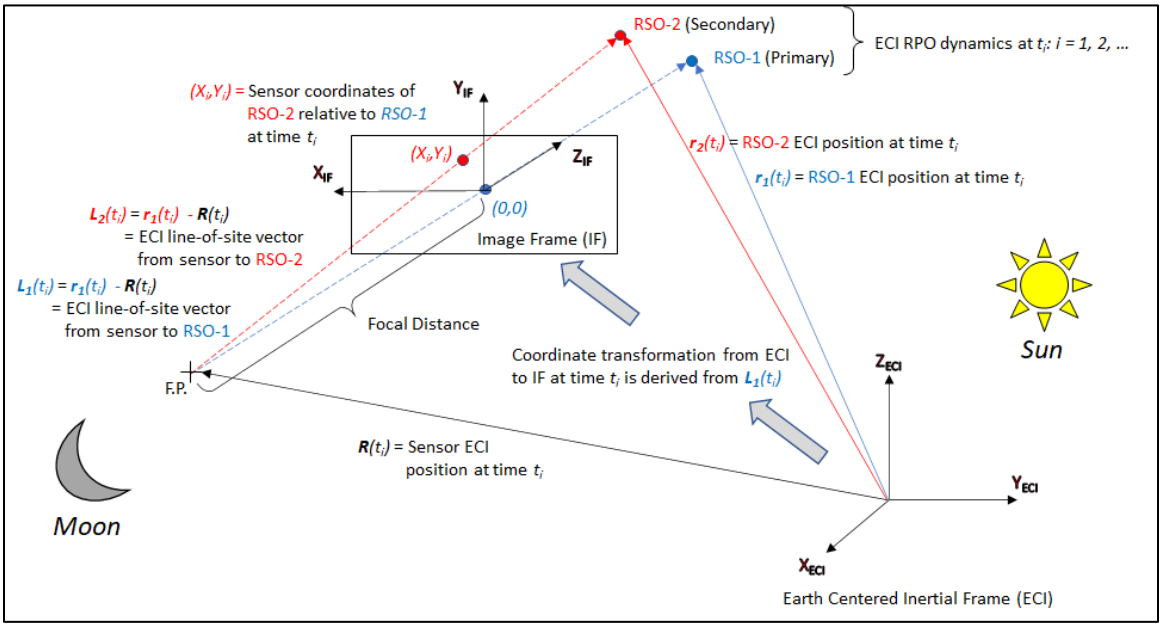

Figure 7. Sensor image-frame coordinates

To ensure a diversity of observing geometries and lighting conditions, the epoch for each data generation trial was varied and the location of the ground or space-based sensor coordinates at epoch were also varied. The methodology for varying the ground-based sensor coordinates is illustrated in Figure 8 where a region below the reference RSO

sub-satellite point is defined in terms of a delta in latitude and longitude. A set of coordinates is sampled from a uniform distribution for each trial and used for generation of the data for that trial run. The distributions of the coordinates used is shown in the histograms in Figure 9 along with the distribution of the trial epoch. This approach is taken to simulate the diversity of expected observation geometries to capture the relative motion from different observing geometries and different lighting conditions and generate a robust, realistic data set.

Similarly, Figure 10 shows the method for generating the initial state used for propagation of the space-based sensor. It is derived from the reference RSO orbit where the true anomaly at epoch is derived from a uniform distribution of a span centered at the true anomaly of the reference, plus or minus a range around that reference. A semi-major axis is sampled to be a band of altitudes above the reference to ensure a slow drift of the sensor relative to the RSO pair. The histograms for the randomly sampled true anomaly and semi-major axis are shown in Figure 11.

Examples trials for the ANIK-F1 vs. ANIK-F1R motion, INTELSAT-901 vs. MEV-1, AMC-11 vs. GALAXY-15 and INTELSAT-36 vs. LUCH (OLYMP) are shown in Figures 12, 13, 14, and 15, respectively. The left-hand figures show the Y vs. X pixel coordinates over the timespan of one trial. The upper right had plot is the time history of the X and Y image coordinates. The EO lighting constraints have been applied and a detection limit of 18 Mv used as one of the constraints. All RSOs were modeled as diffuse spheres and RSO-1 (primary) having a radius of 1 meter and RSO-2 (secondary) having a radius of 0.5 meters. Though not used for this phase of the work, the visual magnitude time histories are shown in the lower right of the figure. Again, the unique patterns exhibited by each of the scenarios can be seen with these examples.

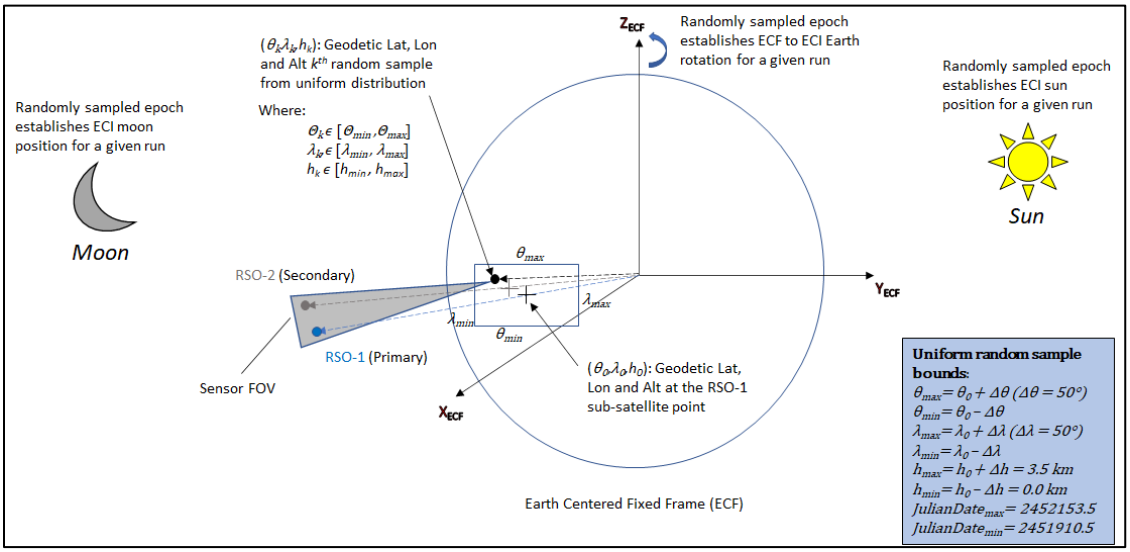

Figure 8. Ground-based sensor coordinates generation methodology

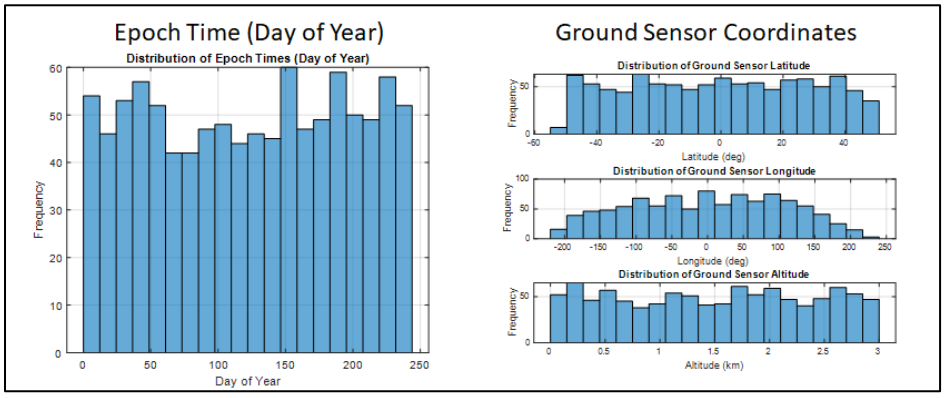

Figure 9. Random epoch and ground-based sensor coordinate distributions

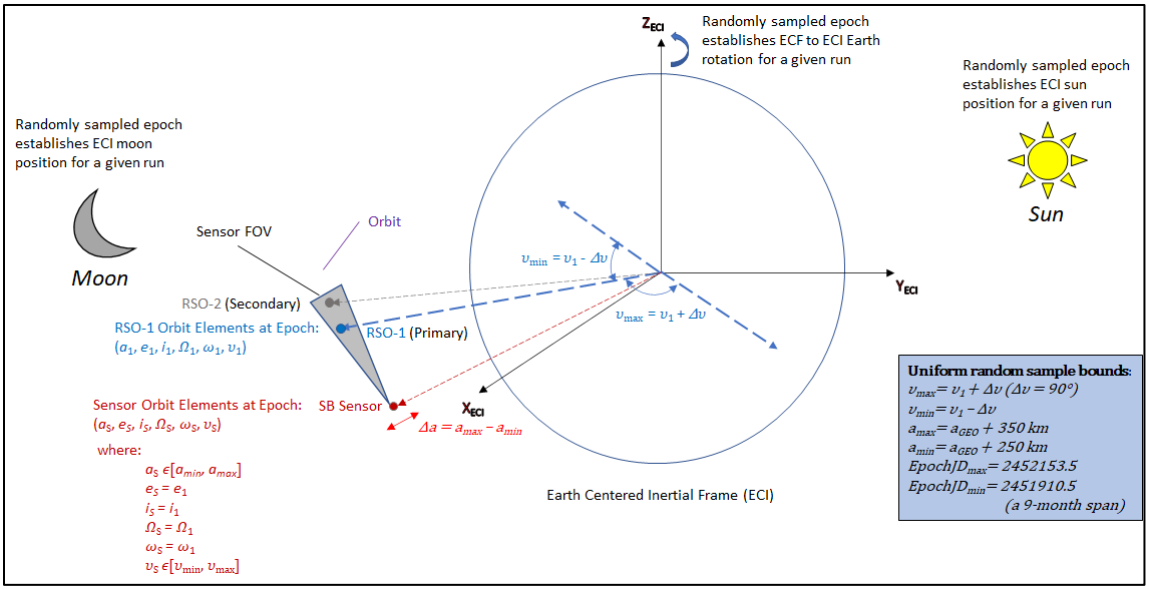

Figure 10. Space-based sensor coordinates generation methodology

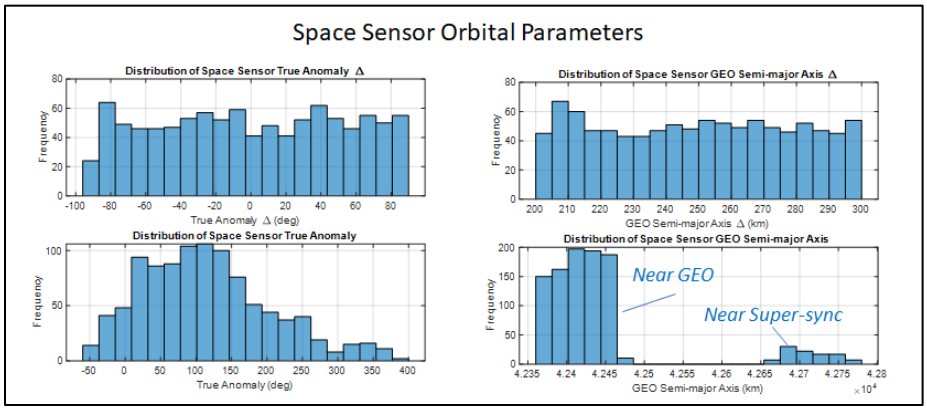

Figure 11. Random space-based orbital parameter distributions

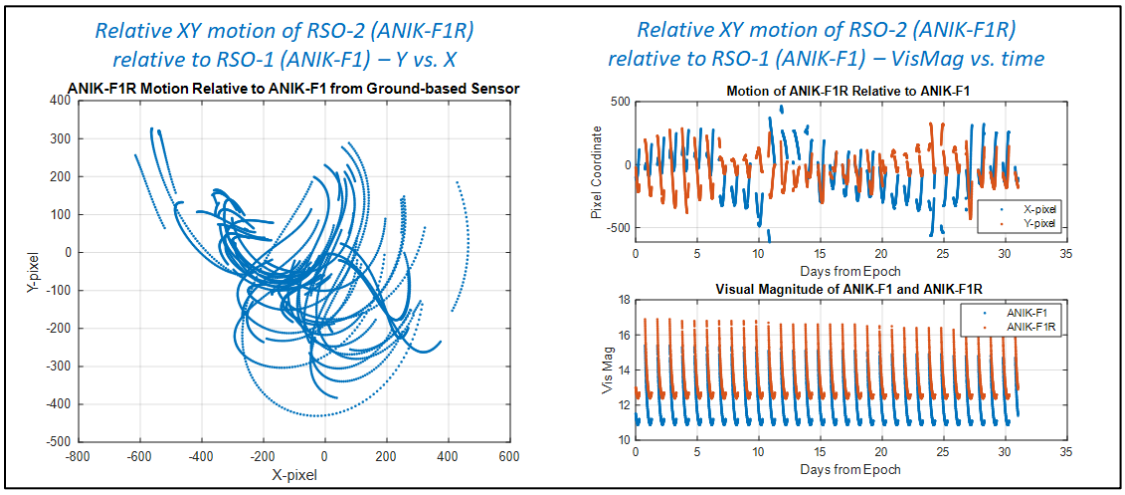

Figure 12. ANIK-F1R vs. ANIK-F1 sensor XY coordinates and magnitudes

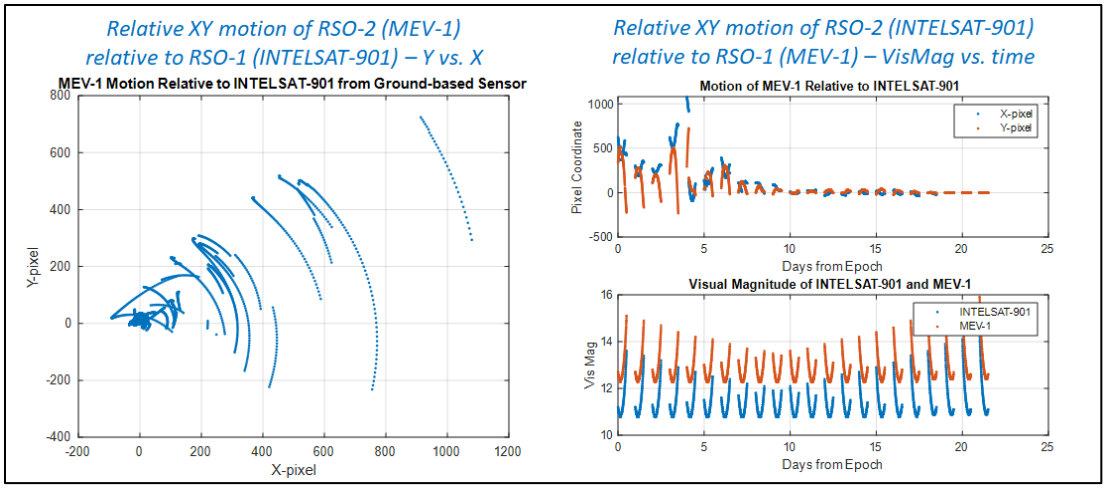

Figure 13. MEV-1 vs. INTELSAT-901 sensor XY coordinates and magnitudes

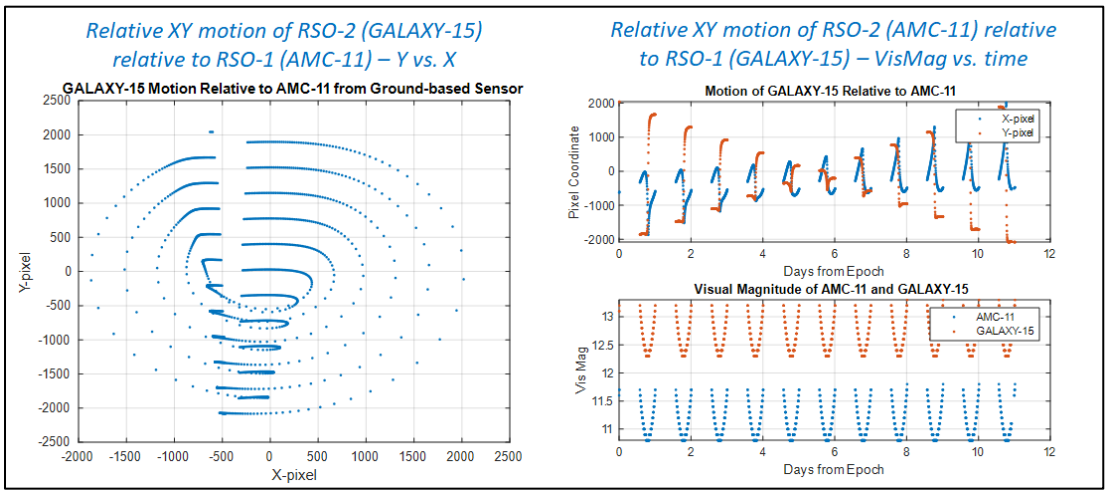

Figure 14. GALAXY-15 vs. AMC-11 sensor XY coordinates and magnitudes

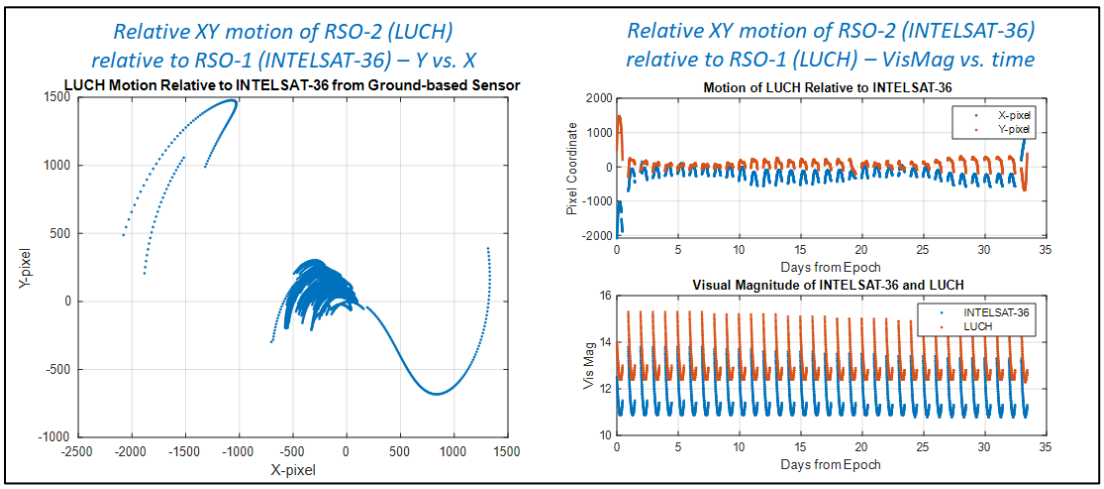

Figure 15. LUCH (OLYMP) vs. INTELSAT-36 sensor XY coordinates and magnitudes

For this work, the observation dataset is comprised of 100 random trial samples generated for each case shown in Table 1 with exception to the RSO Anomaly Case 1 (GALAXY-15 vs. AMC-11). Since there is only a single case, an additional 500 trial samples were generated to ensure proper representation of this scenario. The following section details how the machine learning dataset was prepared and describes the ML model selected.

4. MACHINE LEARNING METHODOLOGY

The scenarios, cases, and quantities of simulated data are provided in Table 1. The RPO with "normal operations" as depicted by the ANIK cluster of GEO satellites is the first scenario where 3 cases result from the combinations of the 3 satellites. The second classification is derived from 2 MEV cooperative docking missions with 2 different INTELSAT satellites. The third classification is represented by the single GALAXY-15 anomaly where it comes within close proximity to AMC-11. There are 2 LUCH encounters represented by the 2 use cases for the "provocative" classification. And, finally, a set of use cases are used to represent "normal" adjacent GEO operations where the relative motion of adjacent GEO satellites is examined. In each case, the state data derived from the TLE histories as previously described is used to generate simulated 2-dimensional observation sets for randomly selected ground and space-based sensors. As described in more detail in the subsequent section, these are partitioned into training, test, and validation datasets to demonstrate the viability of properly classifying the time series of relative motion behavior between two RSOs.

The first step in generating the machine learning training, validation, and test datasets from the simulated observations was to define the structure of an input sample for ML model. In this case, a sample is defined as an observation window, or set of contiguous observations. In the observation dataset gaps naturally occur due to the geometric constraints outlined in the previous section. This divides the observation dataset into a series of observation windows of the RSO pair. These observation windows are then considered as a single sample to form our machine learning datasets. Figure 16 shows the distribution of the number of observations in each observation window. Observation windows with less than 100 observations or greater than 275 observations are filtered out. For observation windows with less than 275 observations, they are zero-padded to create uniformly sized samples and a mask is generated that identifies valid observations.

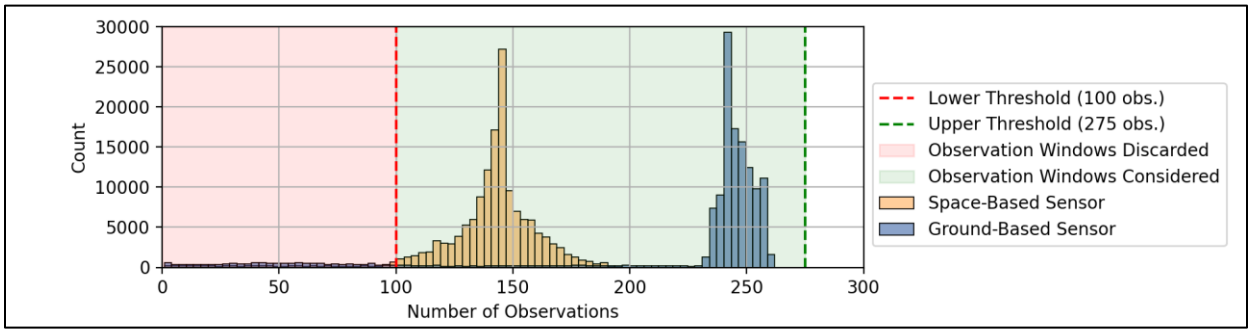

Figure 16. Number of observations per observation window

The leftmost histogram in Figure 17 shows the resulting distribution of observation windows per each scenario. To prevent mixing of trial samples and potential leakage between training, validation, and test datasets, all observation windows within a trial sample are assigned to one of the 3 datasets as shown in the middle histogram of Figure 17. After assigning all trial samples to the respective datasets, observation windows are randomly selected to balance the scenarios with the resulting distributions between the three datasets shown in the rightmost histogram of Figure 17.

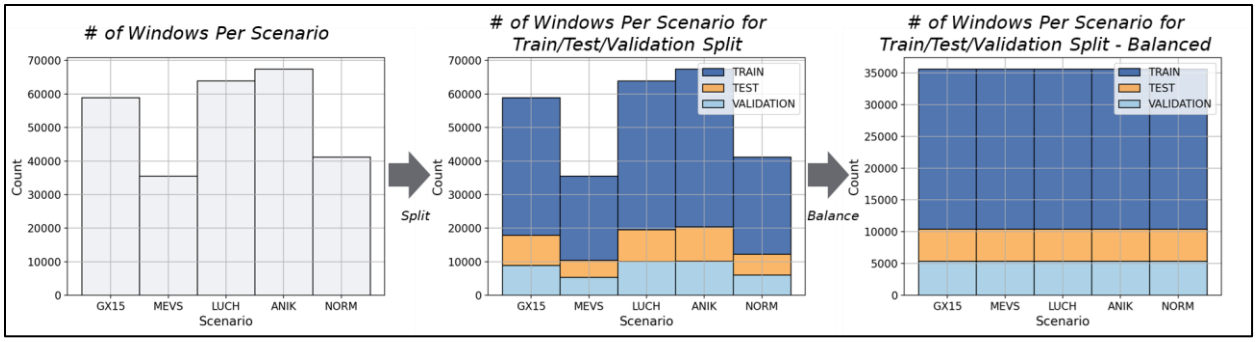

Figure 17. Building the train/test/validation datasets

The data normalization preserves the "shape" of the RSO 2-pixel motion relative to RSO 1 in the sensor frame. When given the relative location of RSO 2 to RSO 1 in pixel space, (x, y), it is converted to polar coordinates and expressed in exponential form, $re^{i\theta}$. Next, the mean radius, r_μ, and standard deviation of the radius, r_σ, of the training dataset are computed. The normalized radius, $\tilde{r}$, is then generated by subtracting the mean radius and dividing the resultant by the standard deviation for all observations in the training/validation/test datasets. This is then converted back to pixel space to derive our normalized observation, $(\tilde{x}, \tilde{y})$, as shown below:

$$\tilde{r} = \frac{r - r_\mu}{r_\sigma} \tag{4-1}$$

$$\tilde{x} = \tilde{r} \cdot cos(\theta) \tag{4-2}$$

$$\tilde{y} = \tilde{r} \cdot \sin(\theta) \tag{4-3}$$

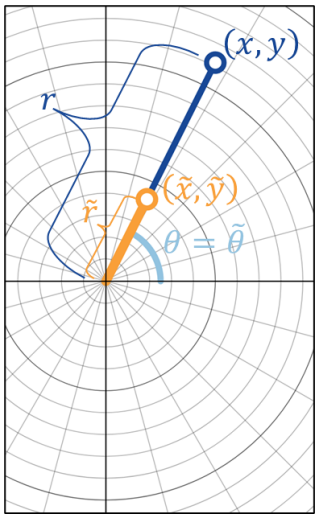

Figure 18. Illustration of an observation before and after normalization of the pixel radius

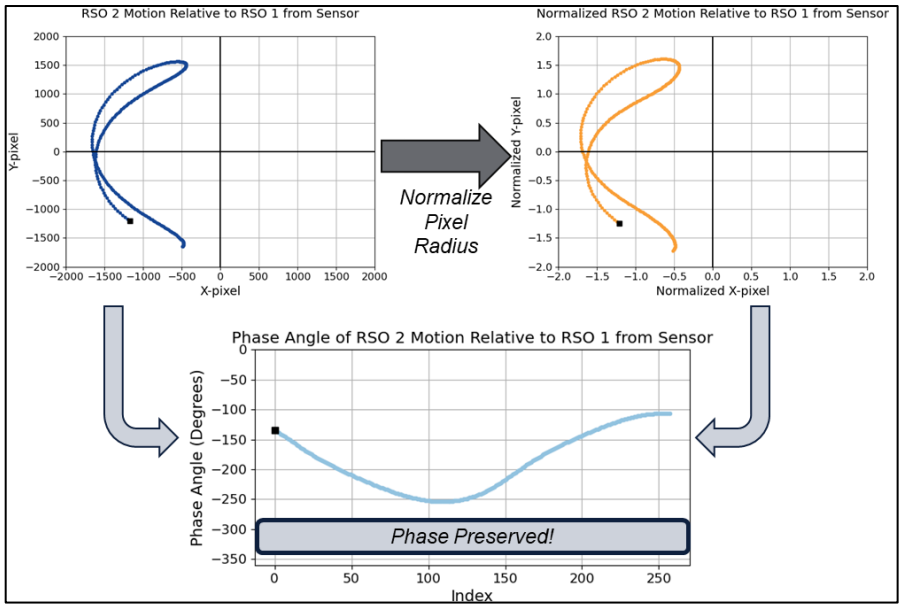

Figure 19. Illustration of the perseverance of phase using our normalization method.

Recent work has shown Transformers are performant for multivariate time series regression and classification [11]. Each of the samples, an observation window of length $W = 275$, can be thought of as a multivariate time series of

our relative X/Y-pixel distances between RSO 1 and RSO 2. The goal is to perform classification of the relative motion behavior captured by this time series.

Classification is performed by a Transformer encoder network shown in Figure 20 [13]. Each time series of X/Y-pixel distances of dimension $W \times 2$, is encoded by a 1-dimensional convolutional layer to match the input dimension of the Transformer encoder, $W \times d_{model}$. Learnable temporal embeddings are added to the encoded observations to provide the encoder temporal context. Additionally, the mask is also provided to the encoder to indicate if the observation is valid, or a part of the zero-pad. The output of the encoder is a latent space representation of the time series of dimension $W \times d_{model}$. This output is averaged across the W observations, accounting for the masked values. Finally, classification is performed by a single-layer fully connected network.

During training, a cosine annealing schedule is used in which the learning rate schedule is gradually decreased from an initial learning rate of 0.0001 and to a non-inclusive minimum of 0 over the 150 training epochs [14]. For the model the Transformer encoder consisted of $N = 6$ encoder layers and dimension, d_{model}, of 512 [13].

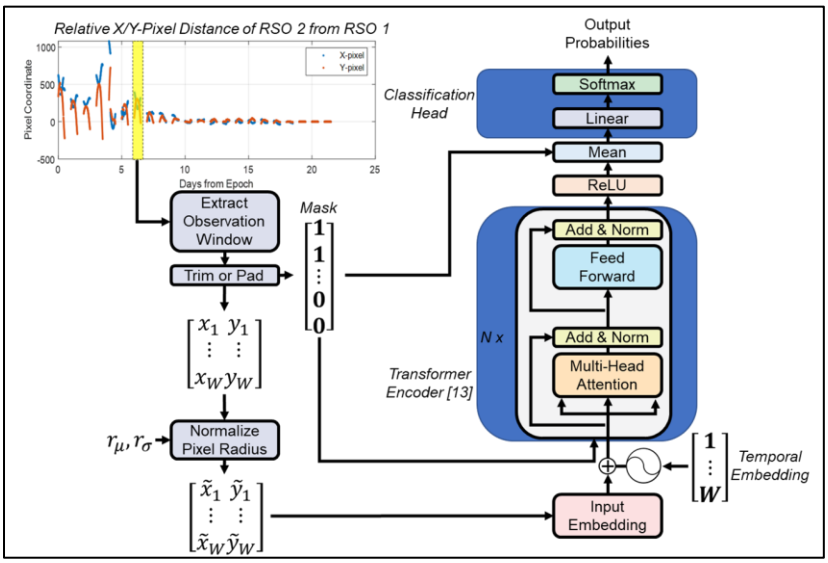

Figure 20. Transformer encoder-based classification architecture.

5. RESULTS

The best model achieved an 85.7% accuracy on the hold out test set. Figure 21 shows the model performance for: ground-based and space-based sensors together (left), only ground-based sensors (center), and only space-based sensors (right). When considering ground-based and space-based sensors together, the model performs best on the GALAXY-15 case with 95.5% accuracy, and the most challenging class is the MEVS case with an accuracy of 78.8%.

The cooperative docking classifications (MEVS) encounter larger misclassifications due to similarities in the relative motion that are observed during distinct phases of the docking as they are very similar to what is observed in the other classes. The resultant confusion matrices show the MEVS observations windows are most commonly misclassified as ANIK (15.4%) with similar misclassification rates observed between ground-based (12.5%) and space-based sensors (18.8%). Figure 22 shows the histogram of the temporal index of the observation window, the index of the first observation in the entire scenario, and the labels assigned to the observation window. From this, it can be seen the majority of the MEVS misclassifications occur from observation windows at the beginning of the simulated scenarios with a temporal index of 3,000 or less. Figure 23 shows that RSO-2 maneuvers to close to RSO-1 at a temporal index between 1,500 and 3,000. However, while the model has difficulty discerning RSO pairs in MEVS scenarios from ANIK early in the scenario, it can accurately differentiate between the two once they are within close proximity. Finally, normal adjacent GEO operations (NORM) cases are misclassified as GALAXY-15 behaviors 15.4% of the time.

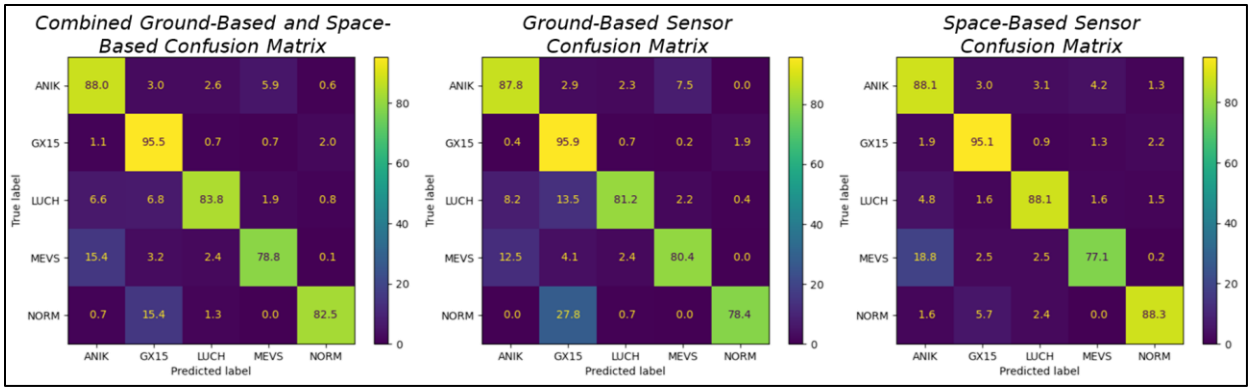

Figure 21. Confusion matrices filtered for all observation windows (left), only ground-based observation windows (middle), and space-based observation windows (right).

Table 2 indicates a high false alarm rate for GALAXY-15. This could be due to the definition of a sample being a single observation window. A single observation window lacks the insight into larger trends (i.e., is an RSO drifting towards another, or are these maneuvers over a shorter time period). Stated in the context of the dynamics at play, GALAXY-15 is drifting slowly towards AMC-11 yet has daily periodicities in the relative motion that are indicative of normal GEOs orbiting in adjacent operational slots. One might miss the drift component and focus on the daily periodicity's indicative of "normal behavior" if the longer temporal drift component is not observed.

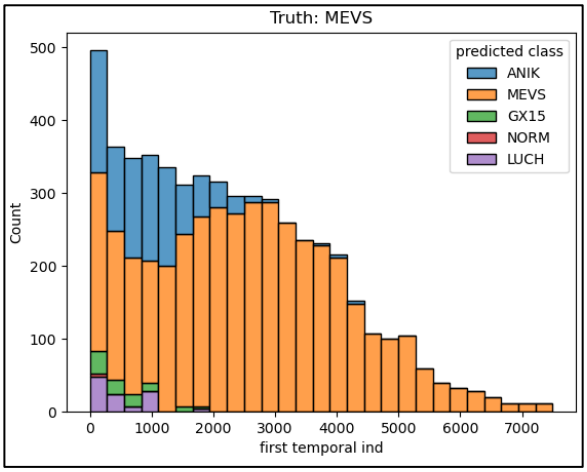

Figure 22. Stacked histogram for first temporal index for all MEVS test sample

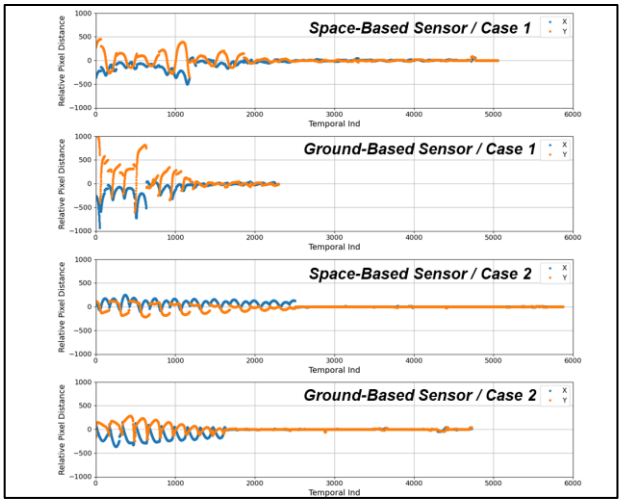

Figure 23. Sample of each MEVS scenario / case where each plot shows RSO pixel difference for X and Y as a function of temporal index

Table 2. Precision and recall metrics

Scenario	Precision	Recall
ANIK	0.79	0.88
GALAXY-15	0.77	0.95
LUCH	0.92	0.84
MEVS	0.90	0.79
NORM	0.96	0.83

6. CONCLUSIONS AND FUTURE WORK

The transformer model demonstrated 85.7% accuracy when classifying RPO behaviors. This indicates reliable classification, but that data segmenting and temporal information are also important, and as intuition dictates, scenario dependent. There are segments of the relative motion that many of the classes have in common, versus relative motion attributes that are unique to each class. Some behavior attributes, i.e., periodic variations in relative motion to orbit period, cause ambiguous classification results due to dynamic attributes in common among the classes. Other unique behavior attributes lend themselves to good classification most importantly, by leveraging temporal information.

Future work will include folding attitude and shape dependent photometry into training to leverage relative attitude motion in the classification. These features could tie to class of RPO behavior and add more information on the intent. Additional machine learning methods can be explored such as hyperparameter tuning and looking at other ways to define a "sample" of the machine learning datasets. For hyperparameter tuning, the default transformer parameters for d_{model} and N were used. Further performance could be gained by tuning these parameters and others (e.g., batch size, number of training epochs, etc.). The focus of this work was on classifying a single observation window. However, scenarios like GALAXY-15 could be better discerned (i.e., less NORM scenarios being falsely classified as GALAXY-15) by providing the Transformer encoder with multiple windows so that the model would potentially learn the slow drift present in the GALAXY-15 scenario and recognize it as not being present in data from the NORM scenario. Analysis of different strategies for data partitioning and sensitivity to partition sizing for each class should be explored to determine if methods can be tuned to detect specific behavior. Trades on amount of data needed to reliably classify can be performed. A more realistic scenario where more than 2 RSOs are in the sensor FOV as was assumed in this work should be analyzed. Lastly, and perhaps most significantly, these methodologies can train on a broader range of behaviors that are established as "norms" of operational space activities and so support verification of those norms towards establishing a safer and more sustainable use of space.

7. ACKNOWLEDGEMENTS

We would like to thank the Stratagem Leadership team – Brian Bontempo, Ben Avicolli, Jason Putnam and Jared Hershman – for having the trust and confidence in supporting this research through precious internal funding. We also extend a sincere thank you to Brian Bontempo and Rad Widman for their valuable reviews and helpful comments. This is a much better paper as a result.

8. REFERENCES

[1] M. Pryak and J. Anderson, "Performance of Northrop Grumman's Mission Extension Vehicle (MEV) RPO Imagers at GEO," in *22nd AMOS Technical Conference*, Wailea, Maui, HI, 2021.

[2] T. Harris, M. Forshaw, M. Lindsay, G. Brydon, A. Lidtke and N. Yarr, "Space Situational Awareness (SSA) activities explored through the ELSA-d mission," in *22nd AMOS Technical Conference*, Wailea, Maui, HI, 2021.

[3] R. Biesbroek, L. Innovecenti, A. Wolahan and S. Serrano, "E.DEORBIT - ESA'S ACTIVE DEBRIS REMOVAL MISSION," in *Proceedings of the 7th European Conference on Space Debris*, Darmstadt, Germany, 2017.

[4] C. Clark, "US, China, Russia Testing New Space War Tactics: Sats Buzzing, Spoofing, Spying," Breaking Defense, 28 October 2021. [Online]. Available: https://breakingdefense.com/2021/10/us-china-russia-test-new-space-war-tactics-sats-buzzing-spoofing-spying/. [Accessed 2022].

[5] C. Dennehy and J. Carpenter, "A Summary of the Rendezvous, Proximity Operations, Docking, and Undocking (RPODU) Lessons Learned from the Defense Advanced Research Project Agency (DARPA) Oribital Express (OE) Demonstration System Mission," National Aeronautics and Space Administration, Hampton, Virginia 23681-2199, 2011.

[6] H. Schaub and J. Junkins, Analytical Mechanics of Space Systems, Fourth Edition ed., AIAA American Institute of Aeronautics & Ast., 2018.

[7] S. Clark, "Galaxy 15 'zombiesat' still alive after expected off date," Spacefilght Now, 15 September 2010. [Online]. Available: https://spaceflightnow.com/news/n1009/15galaxy15/. [Accessed 2022].

[8] D. Hall, "AMOS Galaxy 15 Satellite Observations and Analysis," in *12th AMOS Technical Conference*, Wailea, Maui, HI, 2011.

[9] T. Kelecy and J. Gerber, *Photometric (non-imaging) Data Appplied Towards Distinguising Multiple Objects Observed in a Sensor's Field-of-View*, Wailea, Maui, HI: Non-Imaging Space Object Identification (NISOI) Workshop, 2016.

[10] J. Ianni, C. Sheaff, P. Rocci, G. Thomas and A. Bhopale, "Headline-based Human-Computer Interface to Aggregate Space Indications and Warnings," in *22nd AMOS Technical Conference*, Wailea, Maui, HI, 2021.

[11] G. Zerveas, S. Jayaraman, D. Patel, A. Bhamidipaty and C. Eickhoff, "A Transformer-based Framework for Multivariate Time Series Representation Learning," in *Proceedings of the 27th ACM SIGKDD Conference on Knowledge Discovery and Data Mining*, Virtual Event, Signapore, 2021.

[12] Spacetrack, [Online]. Available: https://space-track.org/documentation.

[13] A. Vaswani, N. Shazeer, N. Parmer, J. Uszkoreit, L. Jones, A. N. Gomez, L. Kaiser and I. Polosukhin, "Attention Is All You Need," in *NIPS 2017*, Long Beach, CA, USA, 2017.

[14] I. Loshchilov and F. Hutter, "SGDR: Stochastic Gradient Descent with Warm Restrats," in *International Conference on Learning Representations*, 2017.

[15] T. Kelecy, E. Lambert, S. Akram and J. Paffett, "Characterization of Resident Space Objects Using Functional Data Analysis," in *21st AMOS Technical Conference*, Wailea, Maui, HI, 2020.

[16] E. Lambert-Gerber, T. Kelecy and J. Balke, "Characterization of Orbital Debris Attributes Using Functional Data Analysis," in *22nd AMOS Technical Conference*, Wailea, Maui, HI, 2021.